Research Article

Vol. 60, No. 16 / 1 June 2021 / Applied Optics 4557

applied optics

Design method for an off-axis reflective anamorphic optical system with aberration balance and constraint control

YUE WU,[1,2] LIPING WANG,[1,3] XU ZHANG,[1,2] JIE YU,[1,3] BO YU,[1,3] AND CHUNSHUI JIN[1,3,*]

[1] Changchun Institute of Optics, Fine Mechanics and Physics, Chinese Academy of Sciences, Changchun, Jilin 130033, China
[2] University of Chinese Academy of Sciences, Beijing 100039, China
[3] State Key Laboratory of Applied Optics, Changchun, Jilin 130033, China
*Corresponding author: jincs@sklao.ac.cn

Received 14 April 2021; revised 27 April 2021; accepted 27 April 2021; posted 28 April 2021 (Doc. ID 427713); published 21 May 2021

This paper proposes a design method for an off-axis reflective anamorphic optical system (ORAOS). This method first applies vector aberration theory to establish a mathematical model to balance the aberration of an ORAOS. It then builds the error function of structural parameters and constraints through spatial ray tracing and grouping design. Next, it introduces automatic adjustment of weight factors for dynamic balance of aberrations and constraints. A particle swarm simulated annealing algorithm is used to iteratively calculate the initial structure of the ORAOS. Finally, we use an extreme ultraviolet (EUV) lithographic projection objective with off-axis six-reflective anamorphic mirrors ($\beta_x = 1/4$, $\beta_y = 1/8$) as an example to verify the effectiveness of this method. We obtain an EUV lithographic anamorphic objective with a numerical aperture of 0.55 and a root mean square wavefront error better than $1/30\lambda$ (Î ≫ = 13.5 nm). © 2021 Optical Society of America

https://doi.org/10.1364/AO.427713

1. INTRODUCTION

An anamorphic optical system is made from double-curvature surfaces that have two mutually perpendicular planes of symmetry, so the system has a different magnification in the two symmetry planes [1–6]. Anamorphic systems have been used in cinema scopes to capture a wide-screen image onto a standard-sized film frame since the 1950s, in laser beam profile control since the 1970s, in semiconductor chip inspection since the 1990s, in 3D displays since 1997, in distortion control of panoramic lenses since 2005, and in high-performance spectrometers since 2008 [6–10]. As a result of the rapid development of the semiconductor industry, lithographic technology has entered the 5 nm level, and extreme ultraviolet (EUV) lithography has attracted considerable attention for use in large-scale integrated circuit processing. The EUV lithographic projection objective, which is the core component of an EUV lithographic system, is a microscopic objective that requires very high imaging quality. Resolution is determined by the Rayleigh resolution criterion, $R = k_1 \frac{\lambda}{\mathrm{NA}}$. To achieve higher resolution, the numerical aperture (NA) of the EUV objective optical system needs to be increased. For high-NA optical systems, it is no longer feasible to maintain 4× reduction, a full field of view, and a 6 in. mask. High-NA optical systems introduce a sharply increasing incident angle, which increases the shadow effect and reduces the aerial image contrast. The solution is to reduce the mask incident angle and increase the demagnification of the projection objective. To combine the full field of view of a $26 \times 33\ \mathrm{mm}^2$ image plane with a 6 in. mask, an anamorphic optical system is used to provide the required demagnification in two mutually perpendicular planes. An anamorphic projection objective with a $4 \times /8\times$ demagnification in the X/Y direction can use a 6 in. mask to achieve a $26 \times 16.5\ \mathrm{mm}^2$ half-field exposure, providing the best productivity and resolution [11–16]. The EUV lithographic projection objective strongly relies on aberration balancing, which poses major challenges to optical designers. Using software to optimize design strongly depends on selecting the initial structure. The construction of this initial structure therefore plays the most important role in designing the optical system [17,18]. For a non-rotationally symmetric system with high imaging quality and multiple constraints, it is essential to construct an initial structure that satisfies the dynamic balance between aberration and multi-constraint control requirements.

Over the past years, the main method for designing an anamorphic optical system has been using a paraxial model to calculate the first-order aberrations of the optical system exhaustively. However, a paraxial search cannot control the constraints effectively. Furthermore, the values that satisfy the constraints can be too small, which strongly affects the calculation efficiency, and the ability of the method to balance aberration is too weak. Wynne, Burfoot, Sands, Yuan, etc. calculated and analyzed the third-order aberration of an anamorphic optical system but did not give specific design examples [1–3,6]. For an

EUV anamorphic optical system, Hans applied group design to an EUV anamorphic optical system by dividing the optical system into two groups but did not provide a specific design method [19]. Li's group proposed combining curvatures for an anamorphic magnification EUV lithographic objective [20]. This method takes a series of control measures to design two coaxial spherical systems to ensure the rationalities of the initial structure and the surfaces after they are combined. The image quality of the anamorphic initial structure is optimized through a gradual process. The constraints of this method are too strict, and the aberration balance problem is not considered; the method completely relies on optical design software to correct aberrations. This has three effects. First, the curvature combination method may filter out numerous qualified solutions, reduce the structural diversity, and make other constraints too tight. Second, the software optimization process may produce large disturbances, leading the structure to deviate too far from the initial structure and making the constraints difficult to control. Finally, the optimization process used by optical design software to balance aberration may increase the residual values of both low-order and high-order aberrations and then increase the residual values of the design.

To solve the problems of aberration balance and constraint control in the anamorphic optical system, this paper proposes a design method for ORAOS. First, this method derives and calculates the third-order aberration of the anamorphic optical system using vector aberration theory. The third-order aberration of the anamorphic optical system is used not only for analysis but also for aberration control during the initial construction. Second, we apply spatial ray tracing to characterize and control constraints, and parameterize the structural parameters, aberration coefficients, and constraints. Third, we introduce automatic adjustment of weight factors to dynamically balance the aberration coefficients and constraint parameters, and establish mathematical models to calculate the corresponding parameters for the ORAOS. A particle swarm simulated annealing algorithm is used to calculate the initial structural parameters. Fourth, a variable step strategy is used to make the optimization converge smoothly and prevent the results from deviating too much from the initial structure. Finally, we complete the design of an off-axis six-reflective anamorphic optical system that is feasible and gives a root mean square (RMS) wavefront error of better than $1/30\lambda$, where λ is the operating wavelength.

2. DESIGN METHOD

A. Group Design

As shown in Fig. 1, we divide the ORAOS into two groups, the objective lens group and the image lens group. The parameters of the optical system mainly include the magnifications in the X and Y directions, β_x and β_y; the center object height y; the center image height y_{im}; the numerical apertures of the object side in the X and Y directions NAO_x and NAO_y; and the image side numerical aperture NA, from which we can obtain $y_{im} = y/\beta_y$, $\mathrm{NAO}_x = \mathrm{NA}/\beta_x$, and $\mathrm{NAO}_y = \mathrm{NA}/\beta_y$. The objective lens group and the image side lens group are spliced together at the intermediate image position, which should obey the principles of object–image matching, pupil matching, and demagnification matching. In the design of an anamorphic optical system, the ratio of the object side numerical apertures for the X and Y directions is 2:1, so the entrance pupil is no longer circular, but elliptical, and the ratio of the entrance pupil diameters for the X and Y directions is 2:1. In the group design, the objective lens group is set as an anamorphic group, and the image side lens group as a fixed lens group. The rays are emitted from the elliptical entrance pupil via the objective lens group to the intermediate image point, forming a rotationally symmetric system. Then, rays are emitted from the intermediate image point via the image lens group to the circular exit pupil. The objective lens group in this study has the anamorphic conic surface expression

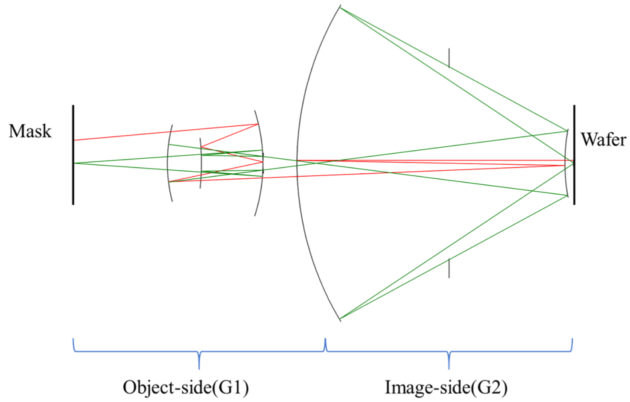

Fig. 1. Schematic of ORAOS.

$$Z = \frac{c_x x^2 + c_y y^2}{1 + \sqrt{1 - (1 + k_x)c_x^2 x^2 - (1 + k_y)c_y^2 y^2}}, \tag{1}$$

where c_x and c_y represent the curvatures of the XZ plane and the YZ plane, respectively, and k_x and k_y represent the cones of the XZ and YZ planes, respectively. From the above principles, ensuring rays in the X/Y direction of the front lens group intersect at the intermediate image point requires an X/Y magnification ratio of 2:1 for the objective lens group, and an entrance pupil diameter ratio of 2:1 for the X and Y directions. Then, the structural parameters of the objective lens and image lens groups are parameterized, and the third-order aberration of the deformable optical system is calculated using vector aberration theory. Spatial ray tracing is applied to control the constraints, including obscurations, lens distances, image telecentricity, lens apertures, the obscuration ratio, and angles of incidence. We then parameterize these constraints.

B. Aberration Analysis

1. Aberration Analysis of the Anamorphic Optical System

The transfer and refraction equations of an anamorphic optical system can be written as [6]

$$\begin{cases} \dfrac{x_j - x_{j-1}}{u_{x,j-1}} = \dfrac{y_j - y_{j-1}}{u_{y,j-1}} = t_{j-1} \\ \dfrac{n_j u_{x,j} - n_{j-1} u_{x,j-1}}{c_{x,j} x_j} = \dfrac{n_j u_{y,j} - n_{j-1} u_{y,j-1}}{c_{y,j} x_j} = -(n_j - n_{j-1}) \end{cases}, \tag{2}$$

where $c_{x,j} = 1/r_{x,j}$, $c_{y,j} = 1/r_{y,j}$ represent the curvatures of surface j of the XZ and YZ planes, respectively; (x_{j-1}, y_{j-1}), (x_j, y_j) represent the coordinates of the intersection points between the ray and surfaces $j-1$ and j, respectively; $(u_{x,j-1}, u_{y,j-1})$, $(u_{x,j}, u_{y,j})$ represent the direction cosines of the ray between surfaces $j-1$ and j and between surfaces j and $j+1$, respectively; t_{j-1} represents the distance between surfaces $j-1$ and j; and (n_{j-1}, n_j) represent the refractive indices between surfaces $j-1$ and j and between surfaces j and $j+1$, respectively.

In the paraxial region, an anamorphic system can be replaced by two independent rotationally symmetric optical systems (RSOSs), each associated with one symmetry plane. In each associated RSOS, we know there are only two independent non-skew paraxial rays, normally taken to be the marginal and chief rays, and any other paraxial ray in the RSOS can be written as their linear combination. It is evident that any skew paraxial ray in an anamorphic system can be fully specified by four non-skew paraxial rays, namely, the x and y marginal rays, the x and y chief rays, and the corresponding x and y RSOS. The proportionality constants of each linear combination are the normalized object and stop coordinates of the arbitrary skew paraxial ray:

$$\begin{cases} \bar{\bar{x}}_j = \rho_x h_{x,j} + H_x \bar{h}_{x,j} \\ \bar{\bar{u}}_{x,j} = \rho_x u_{x,j} + H_x \bar{u}_{x,j} \\ \bar{\bar{y}}_j = \rho_y h_{y,j} + H_y \bar{h}_{y,j} \\ \bar{\bar{u}}_{y,j} = \rho_y u_{y,j} + H_y \bar{u}_{y,j} \end{cases}, \tag{3}$$

where $(\bar{\bar{x}}_j, \bar{\bar{u}}_{x,j}, \bar{\bar{y}}_j, \bar{\bar{u}}_{y,j})$ represents the parameters of an arbitrary paraxial ray in the anamorphic optical system; $(h_{x,j}, u_{x,j})$, $(\bar{h}_{x,j}, \bar{u}_{x,j})$ represent the height and angle of a paraxial marginal ray and chief ray in the x direction on surface j, respectively; $(h_{y,j}, u_{y,j})$, $(\bar{h}_{y,j}, \bar{u}_{y,j})$ represent the height and angle of a paraxial marginal ray and chief ray in the y direction on surface j, respectively; and (H_x, H_y), (ρ_x, ρ_y) represent the normalized object and stop coordinates.

2. *Third-Order Aberration Analysis*

Our third-order aberration analysis is based on vector wave aberration theory [1–5,21,22]:

$$\begin{aligned} W_{klm} &= \sum_j \sum_p \sum_n \sum_m (w_{klm})_j \left(\vec{H}\cdot\vec{H}\right)^p \left(\vec{\rho}\cdot\vec{\rho}\right)^n \left(\vec{H}\cdot\vec{\rho}\right)^m \\ &= \sum_j \sum_p \sum_n \sum_m (w_{klm})_j \left[\left(\vec{H_x}+\vec{H_y}\right)\cdot\left(\vec{H_x}+\vec{H_y}\right)\right]^p \left[\left(\vec{\rho_x}+\vec{\rho_y}\right)\cdot\left(\vec{\rho_x}+\vec{\rho_y}\right)\right]^n \left[\left(\vec{H_x}+\vec{H_y}\right)\cdot\left(\vec{\rho_x}+\vec{\rho_y}\right)\right]^m \\ &= \sum_j \sum_p \sum_n \sum_m (w_{klm})_j \left(H_x^2 + H_y^2\right)^p \left(\rho_x^2 + \rho_y^2\right)^n \left(H_x\cdot\rho_x + H_y\cdot\rho_y\right)^m, \end{aligned} \tag{4}$$

where $k = 2p + m$, $l = 2n + m$, and $k + l = 4$. The aberration of the anamorphic optical system depends on object coordinates (H_x, H_y) and stop coordinates (ρ_x, ρ_y), and is composed of the six invariants H_x^2, H_y^2, ρ_x^2, ρ_y^2, $H_x\rho_x$, $H_y\rho_y$. There are a total of 21 fourth-degree terms, including three piston terms $(H_x^4, H_y^4, H_x^2 \cdot H_y^2)$, two terms calculated twice, and 16 anamorphic third-order aberrations terms:

$$\begin{aligned} W\left(H_x, H_y; \rho_x, \rho_y\right) = &\{D_1\rho_x^4 + D_2\rho_y^4 + D_3\rho_x^2\rho_y^2\} \\ &+ \{D_4 H_x\rho_x^3 + D_5 H_y\rho_x^2\rho_y + D_6 H_x\rho_x\rho_y^2 + D_7 H_y\rho_y^3\} \\ &+ \{D_8 H_x^2\rho_x^2 + D_9 H_y^2\rho_y^2 + D_{10} H_y^2\rho_x^2 + D_{11} H_x^2\rho_y^2 + D_{12} H_x H_y\rho_x\rho_y\} \\ &+ \{D_{13} H_x^3\rho_x + D_{14} H_y^3\rho_y + D_{15} H_x H_y^2\rho_x + D_{16} H_x^2 H_y\rho_y\}. \end{aligned} \tag{5}$$

The third-order aberration coefficients of the anamorphic optical system are expressed as

$$
\left\{
\begin{aligned}
D_1 &= -\tfrac{1}{8}\sum_{j=1}^{k}\left\{\left[A_{x,j}(h_{x,j}\Delta u_{x,j}^2 + c_{x,j}h_{x,j}^2\Delta u_{x,j})\right] + (c_{x,j}^3 - c_{3,j}^3)h_{x,j}^4\Delta n_j\right\} = -\tfrac{1}{8}S_{\mathrm{I}x} \\
D_2 &= -\tfrac{1}{8}\sum_{j=1}^{k}\left\{\left[A_{y,j}(h_{y,j}\Delta u_{y,j}^2 + c_{y,j}h_{y,j}^2\Delta u_{y,j})\right] + (c_{y,j}^3 - c_{5,j}^3)h_{y,j}^4\Delta n_j\right\} = -\tfrac{1}{8}S_{\mathrm{I}y} \\
D_3 &= -\tfrac{1}{4}\sum_{j=1}^{k}\left\{\left[A_{x,j}(h_{x,j}\Delta u_{y,j}^2 + c_{y,j}h_{y,j}^2\Delta u_{x,j})\right] + (c_{x,j}^2c_{y,j} - c_{4,j}^3)h_{x,j}^2h_{y,j}^2\Delta n_j\right\} \\
D_4 &= -\tfrac{1}{6}\sum_{j=1}^{k}\left\{\left[A_{x,j}(\bar{h}_{x,j}\Delta u_{x,j}^2 + c_{x,j}h_{x,j}^2\Delta\bar{u}_{x,j} + 2h_{x,j}\Delta u_{x,j}\bar{u}_{x,j} + 2c_{x,j}h_{x,j}\bar{h}_{x,j}\Delta u_{x,j}) - \psi_x\Delta u_{x,j}^2\right.\right. \\
&\quad \left.\left. +\ 3(c_{x,j}^3 - c_{3,j}^3)h_{x,j}^3\bar{h}_{x,j}\Delta n_j\right]\right\} = -\tfrac{1}{2}S_{\mathrm{II}x} \\
D_5 &= -\tfrac{1}{2}\sum_{j=1}^{k}\left\{\left[A_{x,j}(h_{x,j}\Delta u_{y,j}\bar{u}_{y,j} + c_{y,j}h_{y,j}\bar{h}_{y,j}\Delta u_{x,j}) + (c_{x,j}^2c_{y,j} - c_{4,j}^3)h_{x,j}^2h_{y,j}\bar{h}_{y,j}\Delta n_j\right]\right\} \\
D_6 &= -\tfrac{1}{2}\sum_{j=1}^{k}\left\{\left[A_{x,j}(\bar{h}_{x,j}\Delta u_{y,j}^2 + c_{y,j}h_{y,j}^2\Delta\bar{u}_{x,j}) - \psi_x\Delta u_{y,j}^2 + (c_{x,j}^2c_{y,j} - c_{4,j}^3)h_{x,j}\bar{h}_{x,j}h_{y,j}^2\Delta n_j\right]\right\} \\
D_7 &= -\tfrac{1}{6}\sum_{j=1}^{k}\left\{\left[A_{y,j}(\bar{h}_{y,j}\Delta u_{y,j}^2 + c_{y,j}h_{y,j}^2\Delta\bar{u}_{y,j} + 2h_{y,j}\Delta u_{y,j}\bar{u}_{y,j} + 2c_{y,j}h_{y,j}\bar{h}_{y,j}\Delta u_{y,j}) - \psi_y\Delta u_{y,j}^2\right.\right. \\
&\quad \left.\left. +\ 3(c_{y,j}^3 - c_{5,j}^3)h_{y,j}^3\bar{h}_{y,j}\Delta n_j\right]\right\} = -\tfrac{1}{2}S_{\mathrm{II}y} \\
D_8 &= -\tfrac{1}{4}\sum_{j=1}^{k}\left\{\left[A_{x,j}(h_{x,j}\Delta\bar{u}_{x,j}^2 + c_{x,j}\bar{h}_{x,j}^2\Delta u_{x,j} + 2\bar{h}_{x,j}\Delta u_{x,j}\bar{u}_{x,j} + 2c_{x,j}h_{x,j}\bar{h}_{x,j}\Delta\bar{u}_{x,j}) - 2\psi_x\Delta u_{x,j}\bar{u}_{x,j}\right.\right. \\
&\quad \left.\left. +\ 3(c_{x,j}^3 - c_{3,j}^3)h_{x,j}^2\bar{h}_{x,j}^2\Delta n_j\right]\right\} = -\tfrac{1}{4}(3S_{\mathrm{III}x} + S_{\mathrm{IV}x}) \\
D_9 &= -\tfrac{1}{4}\sum_{j=1}^{k}\left\{\left[A_{y,j}(h_{y,j}\Delta\bar{u}_{y,j}^2 + c_{y,j}\bar{h}_{y,j}^2\Delta u_{y,j} + 2\bar{h}_{y,j}\Delta u_{y,j}\bar{u}_{y,j} + 2c_{y,j}h_{y,j}\bar{h}_{y,j}\Delta\bar{u}_{y,j}) - 2\psi_y\Delta u_{y,j}\bar{u}_{y,j}\right.\right. \\
&\quad \left.\left. +\ 3(c_{x,j}^3 - c_{3,j}^3)h_{x,j}^2\bar{h}_{x,j}^2\Delta n_j\right]\right\} = -\tfrac{1}{4}(3S_{\mathrm{III}y} + S_{\mathrm{IV}y}) \\
D_{10} &= -\tfrac{1}{4}\sum_{j=1}^{k}\left\{\left[A_{x,j}(h_{x,j}\Delta\bar{u}_{y,j}^2 + c_{y,j}\bar{h}_{y,j}^2\Delta u_{x,j})\right] + (c_{x,j}^2c_{y,j} - c_{4,j}^3)h_{x,j}^2\bar{h}_{y,j}^2\Delta n_j\right\} \\
D_{11} &= -\tfrac{1}{4}\sum_{j=1}^{k}\left\{\left[A_{y,j}(h_{y,j}\Delta u_{x,j}^2 + c_{x,j}h_{x,j}^2\Delta u_{y,j})\right] + (c_{x,j}c_{y,j}^2 - c_{4,j}^3)\bar{h}_{x,j}^2h_{y,j}^2\Delta n_j\right\} \\
D_{12} &= -\sum_{j=1}^{k}\left\{\left[A_{x,j}(\bar{h}_{x,j}\Delta u_{y,j}\bar{u}_{y,j} + c_{y,j}h_{y,j}\bar{h}_{y,j}\Delta\bar{u}_{x,j}) - \psi_x\Delta u_{y,j}\bar{u}_{y,j} + (c_{x,j}^2c_{y,j} - c_{4,j}^3)h_{x,j}\bar{h}_{x,j}h_{y,j}\bar{h}_{y,j}\Delta n_j\right]\right\} \\
D_{13} &= -\tfrac{1}{2}\sum_{j=1}^{k}\left\{\left[A_{x,j}(\bar{h}_{x,j}\Delta\bar{u}_{x,j}^2 + c_{x,j}\bar{h}_{x,j}^2\Delta\bar{u}_{x,j}) - \psi_x\Delta\bar{u}_{x,j}^2 + (c_{x,j}^3 - c_{3,j}^3)h_{x,j}\bar{h}_{x,j}^3\Delta n_j\right]\right\} = -\tfrac{1}{2}S_{\mathrm{V}x} \\
D_{14} &= -\tfrac{1}{2}\sum_{j=1}^{k}\left\{\left[A_{y,j}(\bar{h}_{y,j}\Delta\bar{u}_{y,j}^2 + c_{y,j}\bar{h}_{y,j}^2\Delta\bar{u}_{y,j}) - \psi_y\Delta\bar{u}_{y,j}^2 + (c_{y,j}^3 - c_{5,j}^3)h_{y,j}\bar{h}_{y,j}^3\Delta n_j\right]\right\} = -\tfrac{1}{2}S_{\mathrm{V}y} \\
D_{15} &= -\tfrac{1}{2}\sum_{j=1}^{k}\left\{\left[A_{x,j}(\bar{h}_{x,j}\Delta\bar{u}_{y,j}^2 + c_{y,j}\bar{h}_{y,j}^2\Delta\bar{u}_{x,j}) - \psi_x\Delta\bar{u}_{y,j}^2 + (c_{x,j}^2c_{y,j} - c_{4,j}^3)h_{x,j}\bar{h}_{x,j}\bar{h}_{y,j}^2\Delta n_j\right]\right\} \\
D_{16} &= -\tfrac{1}{2}\sum_{j=1}^{k}\left\{\left[A_{y,j}(\bar{h}_{y,j}\Delta\bar{u}_{x,j}^2 + c_{x,j}\bar{h}_{x,j}^2\Delta\bar{u}_{y,j}) - \psi_y\Delta\bar{u}_{x,j}^2 + (c_{x,j}^2c_{y,j} - c_{4,j}^3)\bar{h}_{x,j}^2h_{y,j}\bar{h}_{y,j}\Delta n_j\right]\right\}
\end{aligned}
\right. , \tag{6}
$$

$$
\left\{
\begin{aligned}
A_{x,j} &= n_ju_{x,j} + n_jh_{x,j}c_{x,j} \\
\bar{A}_{x,j} &= n_j\bar{u}_{x,j} + n_j\bar{h}_{x,j}c_{x,j} \\
A_{y,j} &= n_ju_{y,j} + n_jh_{y,j}c_{y,j} \\
\bar{A}_{y,j} &= n_j\bar{u}_{y,j} + n_j\bar{h}_{y,j}c_{y,j}
\end{aligned}
\right. ,
\quad
\left\{
\begin{aligned}
c_{3,j} &= \sqrt[3]{(1+k_{x,j})c_{x,j}^3} \\
c_{4,j} &= \sqrt[3]{\tfrac{1}{2}[(1+k_{x,j})c_{x,j}^2c_{y,j} + (1+k_{y,j})c_{x,j}c_{y,j}^2]} \\
c_{5,j} &= \sqrt[3]{(1+k_{y,j})c_{x,j}^3}
\end{aligned}
\right. ,
$$

$$
\left\{
\begin{aligned}
\psi_x &= n_j(\bar{h}_{x,j}u_{x,j} - h_{x,j}\bar{u}_{x,j}) \\
\psi_y &= n_j(\bar{h}_{y,j}u_{y,j} - h_{y,j}\bar{u}_{y,j})
\end{aligned}
\right. . \tag{7}
$$

3. *Aberration Analysis of the Objective Lens Group (Group 1)*

As shown in Fig. 2, the center object height is y, and the paraxial marginal ray angle of the object is u_1. Rays are emitted from the object point via M_1, M_2, M_3, M_4 to the intermediate image points. The quantities are defined as follows: d_1, d_2, d_3, d_4 represent the lens thicknesses from M_1 to each respective intermediate image point; $h_{x,1}$, $h_{x,2}$, $h_{x,3}$, $h_{x,4}$ and $h_{y,1}$, $h_{y,2}$, $h_{y,3}$, $h_{y,4}$ represent the paraxial marginal ray heights of the XZ and YZ planes at M_1, M_2, M_3, M_4, respectively; $r_{x,1}$, $r_{x,2}$, $r_{x,3}$, $r_{x,4}$ and $r_{y,1}$, $r_{y,2}$, $r_{y,3}$, $r_{y,4}$ represent

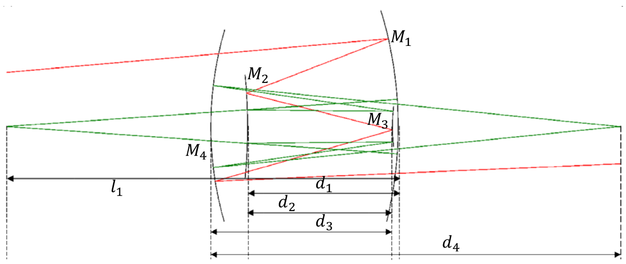

Fig. 2. Schematic of the Group 1 configuration.

the radii of curvature of the XZ and YZ planes at M_1, M_2, M_3, M_4, respectively; $k_{x,1}$, $k_{x,2}$, $k_{x,3}$, $k_{x,4}$ and $k_{y,1}$, $k_{y,2}$, $k_{y,3}$, $k_{y,4}$ represent the cones of the XZ and YZ planes at M_1, M_2, M_3, M_4, respectively; $l_{x,1}$, $l_{x,2}$, $l_{x,3}$, $l_{x,4}$ and $l_{y,1}$, $l_{y,2}$, $l_{y,3}$, $l_{y,4}$ represent the object distances of the XZ and YZ planes at M_1, M_2, M_3, M_4, respectively; and $l'_{x,1}$, $l'_{x,2}$, $l'_{x,3}$, $l'_{x,4}$ and $l'_{y,1}$, $l'_{y,2}$, $l'_{y,3}$, $l'_{y,4}$ represent the image distances of the XZ and YZ planes at M_1, M_2, M_3, M_4, respectively.

Next, we introduce the following parameters on the basis of the paraxial approximation:

$$\begin{cases} \alpha_{x1} = \dfrac{l_{x2}}{l'_{x1}} \approx \dfrac{h_{x2}}{h_{x1}} \\ \alpha_{x2} = \dfrac{l_{x3}}{l'_{x2}} \approx \dfrac{h_{x3}}{h_{x2}} \\ \alpha_{x3} = \dfrac{l_{x4}}{l'_{x3}} \approx \dfrac{h_{x4}}{h_{x3}} \end{cases}, \quad \begin{cases} \alpha_{y1} = \dfrac{l_{y2}}{l'_{y1}} \approx \dfrac{h_{y2}}{h_{y1}} \\ \alpha_{y2} = \dfrac{l_{y3}}{l'_{y2}} \approx \dfrac{h_{y3}}{h_{y2}} \\ \alpha_{y3} = \dfrac{l_{y4}}{l'_{y3}} \approx \dfrac{h_{y4}}{h_{y3}} \end{cases}, \quad \begin{cases} \beta_{x1} = \dfrac{l'_{x1}}{l_{x1}} \\ \beta_{x2} = \dfrac{l'_{x2}}{l_{x2}} \\ \beta_{x3} = \dfrac{l'_{x3}}{l_{x3}} \\ \beta_{x4} = \dfrac{l'_{x4}}{l_{x4}} \end{cases}, \quad \begin{cases} \beta_{y1} = \dfrac{l'_{y1}}{l_{y1}} \\ \beta_{y2} = \dfrac{l'_{y2}}{l_{y2}} \\ \beta_{y3} = \dfrac{l'_{y3}}{l_{y3}} \\ \beta_{y4} = \dfrac{l'_{y4}}{l_{y4}} \end{cases}. \tag{8}$$

For a reflective optical system, $n_1 = n'_2 = n_3 = n'_4 = 1$ and $n'_1 = n_2 = n'_3 = n_4 = -1$. We can obtain the structural parameter expression:

$$\begin{cases} h_{x1} = l_{x1}u_{x1} \\ h_{x2} = \alpha_{x1}l_{x1}u_{x1} \\ h_{x3} = \alpha_{x1}\alpha_{x2}l_{x1}u_{x1} \\ h_{x4} = \alpha_{x1}\alpha_{x2}\alpha_{x3}l_{x1}u_{x1} \end{cases}, \quad \begin{cases} h_{y1} = l_{y1}u_{y1} \\ h_{y2} = \alpha_{y1}l_{y1}u_{y1} \\ h_{y3} = \alpha_{y1}\alpha_{y2}l_{y1}u_{y1} \\ h_{y4} = \alpha_{y1}\alpha_{y2}\alpha_{y3}l_{y1}u_{y1} \end{cases}, \quad \begin{cases} r_{x1} = \dfrac{2\beta_{x1}l_{x1}}{1+\beta_{x1}} \\ r_{x2} = \dfrac{2\alpha_{x1}\beta_{x1}\beta_{x2}l_{x1}}{1+\beta_{x2}} \\ r_{x3} = \dfrac{2\alpha_{x1}\alpha_{x2}\beta_{x1}\beta_{x2}\beta_{x3}l_{x1}}{1+\beta_{x3}} \\ r_{x4} = \dfrac{2\alpha_{x1}\alpha_{x2}\alpha_{x3}\beta_{x1}\beta_{x2}\beta_{x3}\beta_{x4}l_{x1}}{1+\beta_{x4}} \end{cases},$$

$$\begin{cases} r_{y1} = \dfrac{2\beta_{y1}l_{y1}}{1+\beta_{y1}} \\ r_{y2} = \dfrac{2\alpha_{y1}\beta_{y1}\beta_{y2}l_{y1}}{1+\beta_{y2}} \\ r_{y3} = \dfrac{2\alpha_{y1}\alpha_{y2}\beta_{y1}\beta_{y2}\beta_{y3}l_{y1}}{1+\beta_{y3}} \\ r_{y4} = \dfrac{2\alpha_{y1}\alpha_{y2}\alpha_{y3}\beta_{y1}\beta_{y2}\beta_{y3}\beta_{y4}l_{y1}}{1+\beta_{y4}} \end{cases}, \quad \begin{cases} d_1 = \beta_1 l_1 - \alpha_1\beta_1 l_1 \\ d_2 = \alpha_1\beta_1\beta_2 l_1 - \alpha_1\alpha_2\beta_1\beta_2 l_1 \\ d_3 = \alpha_1\alpha_2\beta_1\beta_2\beta_3 l_1 - \alpha_1\alpha_2\alpha_3\beta_1\beta_2\beta_3 l_1 \\ d_4 = \alpha_1\alpha_2\alpha_3\beta_1\beta_2\beta_3 l_1 \end{cases}. \tag{9}$$

Because G1 is an anamorphic group, it should satisfy the following conditions: rays intersect at the intermediate image point in the X/Y direction of G1, the ratio of the X/Y magnifications of G1 is 2:1, and the ratio of the entrance pupil diameters for the X and Y directions is 2:1. Therefore, at least three free variables need to be applied to achieve these conditions. We apply M1 as a rotationally symmetric cone to simplify the calculation. Then, the thickness of G1 is fixed. To achieve the above conditions, we simplify the expressions of some parameters as follows:

$$\begin{cases} \alpha_1 = 1 - \dfrac{d_1}{\beta_1 l_1} \\ \alpha_2 = 1 + \dfrac{d_2}{\beta_2 d_1 - \beta_1\beta_2 l_1} \\ \alpha_3 = \dfrac{d_4}{d_3 + d_4} \end{cases}, \quad \begin{cases} \beta_3 = -\dfrac{d_3 + d_4}{\beta_2 d_1 + d_2 - \beta_1\beta_2 l_1} \\ \beta_4 = -\dfrac{(d_2 + \beta_2(d_1 - \beta_1 l_1))\beta_{G1}}{\beta_1\beta_2(d_3 + d_4)} \end{cases}, \tag{10}$$

where β_{G1} represents the magnification of G1.

4. Aberration Analysis of the Image Lens Group (Group 2)

We will not distinguish the difference in the X/Y directions in G2 because it is an RSOS. As shown in Fig. 3, the center object height of the image lens group is y_5, the center image height of the image lens group is y_{im}, the stop is located between M_5 and M_6, and the object paraxial marginal ray angle of the image lens group is u_5. Rays are emitted from the intermediate image point via M_5 and M_6 to the image point. The other quantities are defined as follows: d_5 and d_6 represent the lens thicknesses from M_5 to M_6 and M_6 to the image plane, respectively; h_5 and h_6 represent the paraxial marginal ray heights at M_5 and M_6, respectively; r_5, r_6 and k_5, k_6 represent the radii of curvature and the cones of M_5 and M_6, respectively; l_5, l_6 and l_5', l_6' represent the object distances and image distances of M_5 and M_6, respectively.

On the basis of the paraxial approximation, we now introduce the following parameters:

$$\alpha_5 = \frac{l_6}{l_5'} \approx \frac{h_6}{h_5}, \quad \begin{cases} \beta_5 = \dfrac{l_5'}{l_5} \\ \beta_6 = \dfrac{l_6'}{l_6} \end{cases}. \tag{11}$$

For a reflective optical system, $n_5 = n_6' = 1$, $n_5' = n_6 = -1$, and $h_5 = l_5 u_5, h_6 = \alpha_1 l_5 u_5$.

According to paraxial optical theory, we can also obtain the following expressions for the radii of curvature and thicknesses:

$$\begin{cases} r_5 = \dfrac{2\beta_5 l_5}{1+\beta_5} \\ r_6 = \dfrac{2\alpha_5\beta_5\beta_6 l_5}{1+\beta_6} \end{cases}, \quad \begin{cases} d_5 = \beta_5 l_5 - \alpha_5\beta_5 l_5 \\ d_6 = \alpha_5\beta_5\beta_6 l_5 \end{cases}. \tag{12}$$

The expression for the distance between the entrance pupil position and M_5 in Group 2 is

$$l_{\mathrm{enpG2}} = \frac{\beta_5 l_5(-1-\beta_6+\alpha_5)}{\alpha_5(1+\beta_5)-\beta_5(1+\beta_6)}. \tag{13}$$

C. Group Matching

From the principles of object–image matching, pupil matching, and demagnification matching, we can obtain the following expressions:

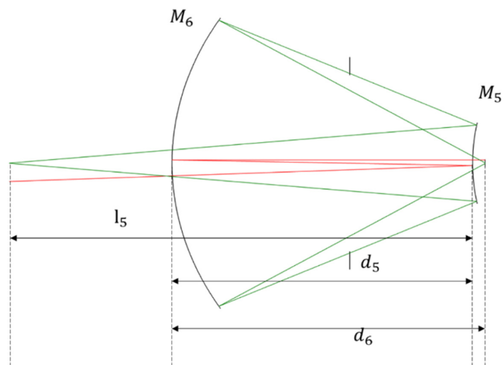

Fig. 3. Schematic of the Group 2 configuration.

$$\begin{cases} \beta_x = \beta_{x1}\beta_{x2}\beta_{x3}\beta_{x4}\beta_5\beta_6 \\ \beta_y = \beta_{y1}\beta_{y2}\beta_{y3}\beta_{y4}\beta_5\beta_6 \\ y_5 = \dfrac{y_{im}}{\beta_5\beta_6} \\ u_5 = \dfrac{u_1}{\beta_1\beta_2\beta_3\beta_4} \end{cases}. \tag{14}$$

Compared with the rotationally symmetric system, some parameters cannot be expressed using the simplified formula. The structural parameters are more complicated than those of the anamorphic optical system. Therefore, we solve the mathematical model numerically instead of analytically.

3. ERROR FUNCTION CALCULATION FOR THE INITIAL STRUCTURE USING AN IMPROVED PARTICLE SWARM SIMULATED ANNEALING ALGORITHM

Using the aberration theory presented above, we obtain the structural parameters and the third-order aberration coefficients of an ORAOS. We then apply real ray tracing and calculate the optical system constraints, including obscurations, lens thicknesses, image telecentricity, lens apertures, the obscuration ratio, and angles of incidence. To balance the third-order aberrations and control constraints, we introduce automatic adjustment of weight factors, and then establish a mathematical model of the above parameters. The error function of the model can be expressed as

$$\begin{aligned} F &= f(\alpha_{x1\_x5}, \alpha_{y1\_y5}, \beta_{x1\_x6}, \beta_{y1\_y6}, k_{x1\_x6}, k_{y1\_y6}) \\ &= \sum_{i=1}^{16} |\omega_i \cdot D_i| + |\text{constraints}| \\ &= \sum_{i=1}^{16} |\omega_i \cdot D_i| + |\omega_{j,1} \cdot \text{Obscuration}| \\ &\quad + |\omega_{j,2} \cdot \text{BWD}| + |\omega_{j,3} \cdot \text{TEL}| + |\omega_{j,4} \cdot \text{RATIO}| \\ &\quad + |\omega_{j,5} \cdot \text{APE}| + \omega_{j,6} \cdot \text{AOI}| + \omega_{j,7} \cdot \text{DIS}|, \end{aligned} \tag{15}$$

where *constraints* in the equation represent the constraints listed above; Obscuration, BWD, TEL, RATIO, AOI, APE, and DIS represent the obscurations, back working distance, image telecentricity, obscuration ratio, maximum aperture, maximum angle of incidence, and distances of mirrors of the optical system, respectively; and ω represents the weight factors. The error function F reflects the value of the third-order aberrations of the optical system and the ability of the system to control these constraints. A smaller value of F indicates smaller third-order aberrations in the initial structure, better control of the constraints, and greater potential to achieve high imaging quality.

Therefore, the essential approach to solve for the initial structure depends on the method used to solve for the minimum value of the error function, and the physical process of solving for the structural parameters of the optical system is thus transformed into a mathematical process to solve for the minimum value of the parameter error function. The main goal is to determine how to solve for the minimum values of the high-dimensional non-linear parameter equations, which include constraints. A particle swarm simulated annealing algorithm offers the following advantages: fast convergence, an ability to jump out of local minima effectively, and a global optimization scheme that does not rely on the initial values and is thus suitable for high-dimensional non-linear optimization [18,23,24].

In this paper, there are 16 third-order aberration terms for the anamorphic optical system. To balance the third-order aberration, each term should be controlled to remain small enough. It is difficult to directly find the exact solution that satisfies the constraints using the particle swarm simulated annealing algorithm. We introduce weight factors to get a smaller F and keep the third-order aberration small enough (1E-2), but it is also difficult to find the exact weight factor to calculate the model. The key to solving this model is to find the weight factor that satisfies the above constraints. An auto-adjustment weight factor is applied to calculate the model. If any third-order aberration or constraint term has not satisfied its condition, we auto-increase the weight of this term in the next iteration. Using this method, we can get the initial structure that satisfies the constraints of the mathematical model. As shown in Fig. 4, the main algorithm for the design process is as follows:

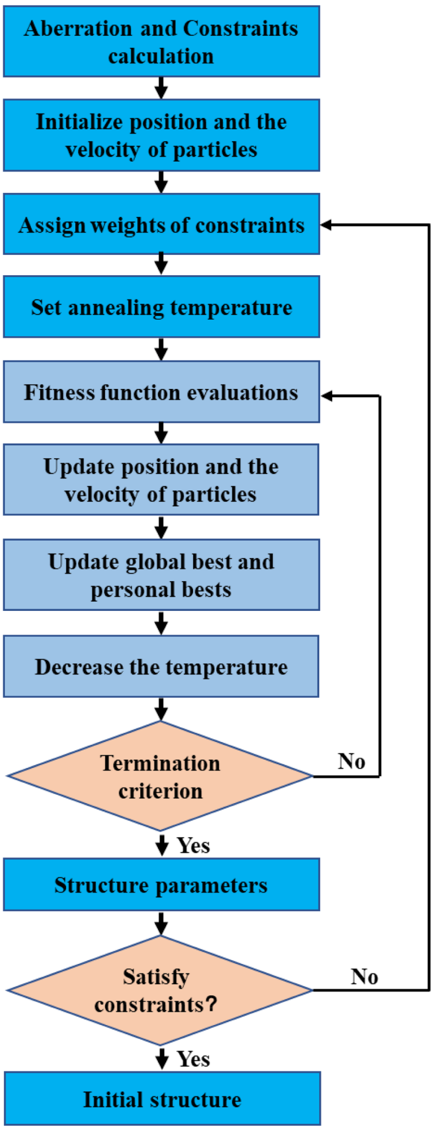

Fig. 4. Flow chart for the improved particle swarm simulated annealing algorithm.

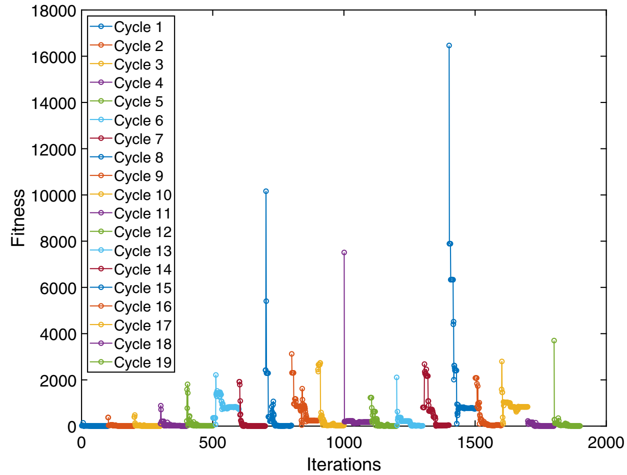

Fig. 5. Convergence curve of the evaluation function for each weight adjustment.

Step 1: Calculate the parameters of the off-axis six-mirror optical system and randomly initialize the positions and velocities of the particles in the population.

Step 2: Assign weights to all constraints in the model.

Step 3: Set the initial temperature. A higher initial temperature increases the probability of obtaining a high-quality solution, but the time required also increases. Therefore, the process for determining the initial temperature should consider both the calculation efficiency and the optimization quality.

Step 4: Evaluate the fitness of each particle and calculate the individual best value and the global best value; the individual best value represents the best solution found for each particle. Then find a global value from these best solutions, which is called the global best value solution.

Step 5: Use the simulated annealing algorithm and the particle swarm algorithm to update the position and the velocity of each particle.

Step 6: On the basis of the fitness value, update the individual best value and the global best value solution for each particle.

Step 7: This is the cooling stage. As T decreases, the algorithm becomes stable, and the probability of selecting a poor solution thus decreases. Finally, T drops to the condition required to terminate the iteration.

Step 8: This is the termination condition. If the termination condition is met (i.e., the error is good enough or the maximum number of cycles has been reached), then exit; otherwise, return to step 4.

Step 9: Calculate the values of the current structural parameters and constraints. If the termination condition is met (i.e., the constraints satisfy the conditions or the maximum number of cycles has been reached), then exit; otherwise, return to step 2.

Step 10: From the calculation results based on the algorithm, we obtain the initial structural parameters of the ORAOS.

The initial structure of the ORAOS is solved using the improved particle swarm simulated annealing algorithm. The main parameters for this algorithm are the number of particles,

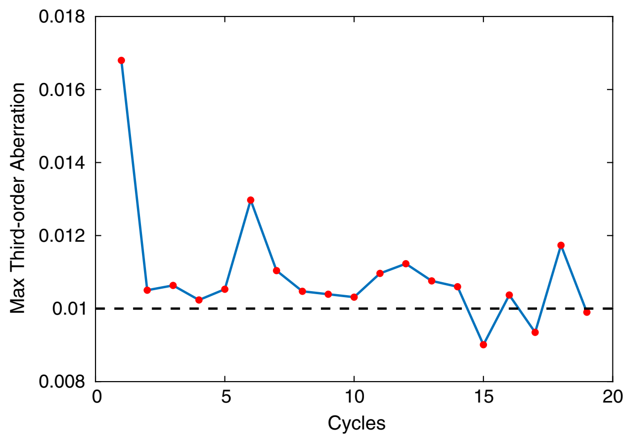

Fig. 6. Distribution of maximum third-order aberration coefficients for each weight adjustment.

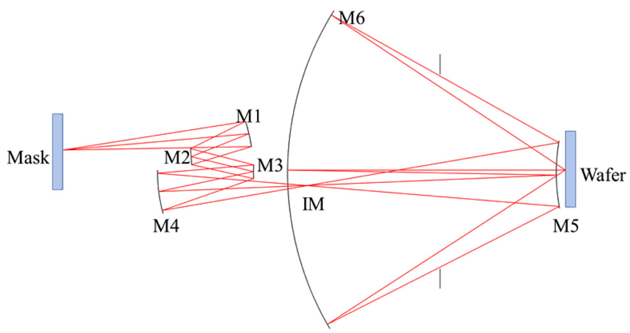

Fig. 7. Schematics of the initial ORAOS structures.

$N = 2000$; the learning factors, $c_1 = 2.05$ and $c_2 = 2.05$; the annealing constant, 0.42; and the maximum number of iterations, $M = 100$. Figure 5 shows the convergence curve of the evaluation function for each weight adjustment. Each point in the curve is the global best error at the specified iteration in each cycle. The error function decreases after 19 cycles (1900 iterations) and converges to a low value close to zero. Figure 6 shows the distribution of the maximum third-order aberration coefficients for each weight adjustment. The third-order aberration is controlled in the first 15 cycles, but other constraints do not satisfy the conditions. There is a dynamic balance between aberrations and constraints from the 15th to the 19th cycle. The diagram of the initial structure is shown in Fig. 7.

4. OPTIMIZATION AND PERFORMANCE

We use an anamorphic aspherical surface to further optimize the designs of the initial structures shown above. We first add high-order coefficients to the anamorphic aspherical surfaces, and then we control the steps for the disturbances for each variable during the optimization process (where a step that is too large may skip an extreme value, and a step that is too small may fall into a local minimum). Using these principles, we optimize the above-mentioned initial structures, but the image quality is too poor. To get more degrees of freedom of optimization, we expand the anamorphic aspherical coefficients to the 16th

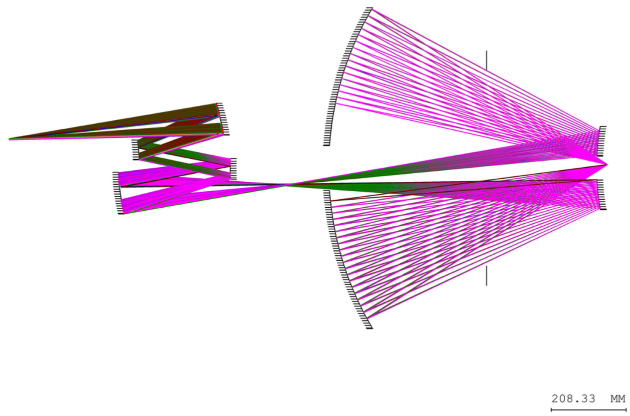

Fig. 8. Schematic of the optimized ORAOS structure.

Table 1. ORAOS Specifications

Parameter	Performance
Wavelength (nm)	13.5
Numerical Aperture NA	0.55
Field of View (mm × mm)	26 × 0.5 Rectangle
Reduction Ratio	$M_x = 4$, $M_y = 8$
Wavefront Error RMS (λ)	0.031
Chief Ray Angle on Mask (°)	5.35
Max Distortion (nm)	2
Max Image Telecentricity (mrad)	0.35
Total Track (mm)	1667
Obscuration ratio	27%

order, but it is still difficult to achieve a high-quality anamorphic optical system design.

To get more degrees of freedom to balance the asymmetric aberration, an XY polynomial surface is applied to optimize further. The expression is

$$Z = \frac{cr^2}{1 + \sqrt{1 - (1+k)c^2 r^2}} + \sum_{j=2}^{66} C_j x^m y^n,$$

$$j = \frac{(m+n)^2 + m + 3n}{2} + 1. \quad \textbf{(16)}$$

We first convert the initial structures to an XY polynomial and perform a Taylor expansion of Eq. (1) to keep the third-order aberration fixed. The object field size is 104 mm × 8 mm, and the length in the X direction is much larger than in the Y direction. The coefficients of odd orders of x are set to zero to simplify the optimization process and improve its efficiency. Using the XY polynomial surface, we obtain an ORAOS design with high imaging quality. Figure 8 shows the design layout for this ORAOS, and the specific system parameters are given in Table 1. Figure 9 shows the distribution of distortions in the full image field. Figure 10 shows the distribution of the RMS wavefront error in the full image field.

Figure 11 shows the modulation transfer function curve which is close to the diffraction limit.

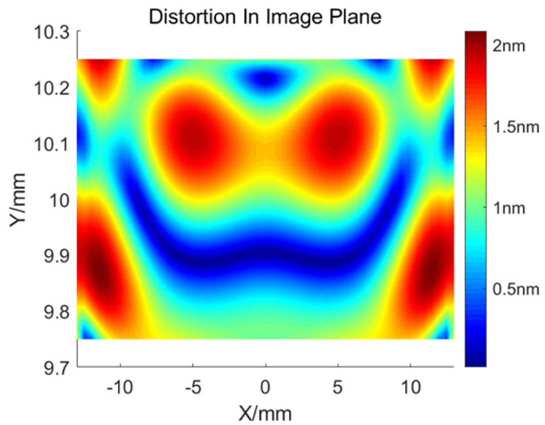

Fig. 9. Distribution of distortions in the full image field.

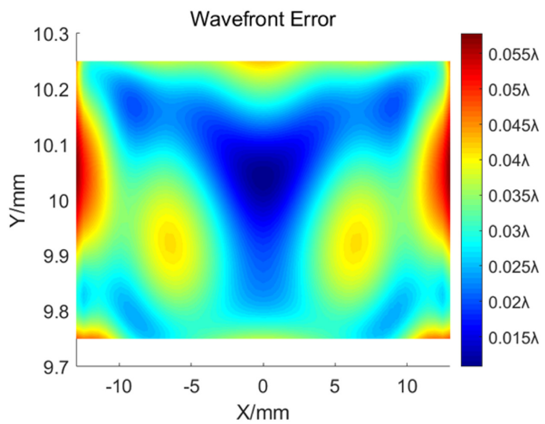

Fig. 10. Distribution of the RMS wavefront error in the full image field.

5. CONCLUSIONS

This paper has proposed a fast and effective method of designing an off-axis reflective anamorphic optical system. First, we calculated the third-order aberration of the ORAOS using vector aberration theory, and then used spatial ray tracing and group design to parameterize the structural parameters, aberration coefficients, and constraints of the anamorphic optical system. Second, automatically adjusted weighting factors were introduced to dynamically balance the aberrations and constraints. A mathematical model to calculate the ORAOS parameters was established. A particle swarm simulated annealing algorithm was used to iteratively solve the error function, quickly and effectively realizing the initial structural design for aberration balance and multi-constraint control. Finally, we completed the design of the ORAOS with suitable engineering feasibility to give an RMS wavefront error of better than $1/30\lambda$.

To obtain more degrees of freedom, vector aberration theory was applied to an off-axis tilted component optical system. This method can be extended to an off-axis tilted component multi-reflection anamorphic optical system. The method can realize an initial structure of such a system that satisfies aberration balance and multi-constraint control. This provides a good starting point for achieving very high imaging quality for the off-axis tilted component multi-reflection anamorphic optical system.

Funding. National Natural Science Foundation of China (61605201).

Disclosures. The authors declare no conflicts of interest.

Data Availability. Data underlying the results presented in this paper are not publicly available at this time but may be obtained from the authors upon reasonable request.

REFERENCES

1. C. G. Wynne, "The primary aberrations of anamorphotic lens systems," Proc. Phys. Soc. Sect. B **67**, 529–537 (1954).
2. J. C. Burfoot, "Third-order aberrations of 'doubly symmetric' systems," Proc. Phys. Soc. Sect. B **67**, 523–528 (1954).
3. P. J. Sands, "Aberration coefficients of double-plane-symmetric systems," J. Opt. Soc. Am. **63**, 425–430 (1973).

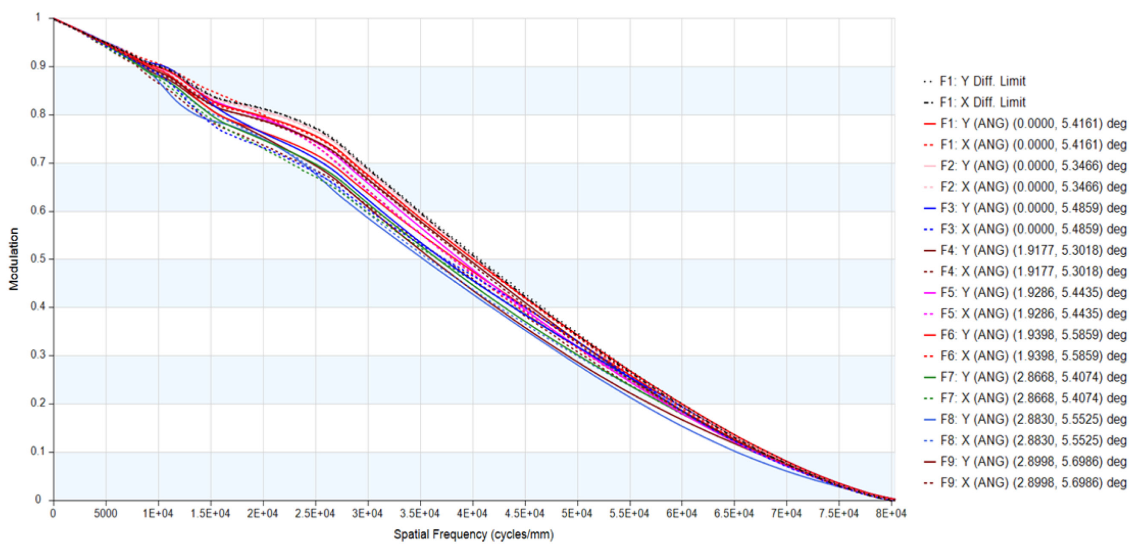

Fig. 11. Modulation transfer function (MTF).

4. J. M. Sasian, “How to approach the design of a bilateral symmetric optical system,” Opt. Eng. **33**, 2045–2061 (1994).
5. J. M. Sasian, “Double-curvature surfaces in mirror system design,” Opt. Eng. **36**, 183–188 (1997).
6. S. Yuan and J. Sasian, “Aberrations of anamorphic optical systems I: the first-order foundation and method for deriving the anamorphic primary aberration coefficients,” Appl. Opt. **48**, 2574–2584 (2009).
7. T. Kasuya, T. Suzuki, and K. Shimoda, “A prism anamorphic system for Gaussian beam expander,” Appl. Phys. **17**, 131–136 (1978).
8. K. Matsumoto and T. Honda, “Research of 3D display using anamorphic optics,” Proc. SPIE **3012**, 199–207 (1997).
9. J. Gauvin, M. Doucet, M. Wang, S. Thibault, and B. Blanc, “Development of new family of wide-angle anamorphic lens with controlled distortion profile,” Proc. SPIE **5874**, 587404 (2005).
10. R. C. Swanson, T. S. Moon, C. W. Smith, M. R. Kehoe, S. W. Brown, and K. R. Lykke, “Anamorphic imaging spectrometer,” Proc. SPIE **6940**, 694010 (2008).
11. J. van Schoot, K. van Ingen Schenau, C. Valentin, and S. Migura, “EUV lithography scanner for sub-8nm resolution,” Proc. SPIE **9422**, 94221F (2015).
12. L. Wischmeier, P. Gräupner, P. Kürz, W. Kaiser, J. Van Schoot, J. Mallmann, J. de Pee, and J. Stoeldraijer, “High-NA EUV lithography optics becomes reality,” Proc. SPIE **11323**, 1132308 (2020).
13. E. van Setten, G. Bottiglieri, J. McNamara, J. van Schoot, K. Troost, J. Zekry, T. Fliervoet, S. Hsu, J. Zimmermann, M. Roesch, B. Bilski, and P. Graeupner, “High NA EUV lithography: Next step in EUV imaging,” Proc. SPIE **10957**, 1095709 (2019).
14. A. Burbine, Z. Levinson, A. Schepis, and B. W. Smith, “Study of angular effects for optical systems into the EUV,” Proc. SPIE **9048**, 90482N (2014).
15. K. van Ingen Schenau, G. Bottiglieri, J. van Schoot, J.-T. Neumann, and M. Roesch, “Imaging performance of the EUV high NA anamorphic system,” Proc. SPIE **9661**, 96610S (2015).
16. P. A. Kearney, O. Wood, E. Hendrickx, G. McIntyre, S. Inoue, F. Goodwin, S. Wurm, J. van Schoot, and W. Kaiser, “Driving the industry towards a consensus on high numerical aperture (high-NA) extreme ultraviolet (EUV),” Proc. SPIE **9048**, 90481O (2014).
17. L. Jun, W. Huang, and F. Hongjie, “A novel method for finding the initial structure parameters of optical systems via a genetic algorithm,” Opt. Commun. **361**, 28–35 (2016).
18. Y. Wu, L. Wang, J. Yu, B. Yu, and C. Jin, “Design method for off-axis aspheric reflective optical system with extremely low aberration and large field of view,” Appl. Opt. **59**, 10185–10193 (2020).
19. H. Mann, “Imaging optics, microlithography projection exposure apparatus having same and related methods.pdf,” U.S. patent 9,013,677 (21 April 2015).
20. Y. Liu, Y. Li, and Z. Cao, “Design of anamorphic magnification high-numerical aperture objective for extreme ultraviolet lithography by curvatures combination method,” Appl. Opt. **55**, 4917–4923 (2016).
21. R. V. Shack and K. Thompson, “Influence of alignment errors of a telescope system on its aberration field,” Proc. SPIE **0251**, 146–153 (1980).
22. S. Yuan and J. Sasian, “Aberrations of anamorphic optical systems III: The primary aberration theory for toroidal anamorphic systems,” Appl. Opt. **49**, 6802–6807 (2010).
23. H. Qin, “Particle swarm optimization applied to automatic lens design,” Opt. Commun. **284**, 2763–2766 (2011).
24. F. Javidrad and M. Nazari, “A new hybrid particle swarm and simulated annealing stochastic optimization method,” Appl. Soft Comput. **60**, 634–654 (2017).

169.236.236.7 {ts '2022-06-08 07:47:11'}